ACS APPLIED POLYMER MATERIALS

Article

Cite This: ACS Appl. Polym. Mater. 2019, 1, 1547−1558

pubs.acs.org/acsapm

Injection Molding of Superhydrophobic Submicrometer Surface Topography on Macroscopically Curved Objects: Experimental and Simulation Studies

Wei Li Lee,[†] Dong Wang,[†,§] Jumiati Wu,[†] Qi Ge,[†,‡] and Hong Yee Low*[,†]

[†]Digital Manufacturing and Design Centre (DManD) and [‡]Science and Math Cluster, Singapore University of Technology and Design, 8 Somapah Road, 487372 Singapore

[§]Robotics Institute, School of Mechanical Engineering, Shanghai Jiao Tong University, Shanghai 200240, China

Supporting Information

ABSTRACT: Micro- and nanoscale surface topographies that give rise to superhydrophobic surfaces have been achieved mostly on 2-dimensional planar objects. Increasing interests in superhydrophobic surfaces on consumer products, optics, and biomedical devices demand topographic patterning on free-form nonplanar surfaces via a high throughput manufacturing process such as injection molding. However, successes in high-resolution (submicrometer) injection molding have been limited to flat and planar objects. A challenge associated with achieving submicrometer surface resolution on a 3-dimensional curved object lies in the control of the replication process in a multiscale mold cavity and the nonuniform temperature and pressure distribution over a macroscopically curved mold insert. Here, a two-step simulation approach is employed to investigate the replication of polymer in the macroscopic and submicrometer cavities. Both simulation and experimental data revealed the effects of holding pressure, mold temperature, and macroscopic curvature on polymer filling percentage and replication uniformity over the entire curved surface. Injection-molded PP with macroscopic curvature and submicrometer surface pattern has been achieved with a high yield and pattern uniformity above 95%. The superhydrophobic property, specifically, spontaneous dewetting of water droplet on curved PP, was demonstrated on anisotropic 300 nm grating and isotropic 250 nm pillar structures. The results presented here can be adopted for development and rapid prototyping of 3-dimensional complex-shaped polymers with superhydrophobic surface topography.

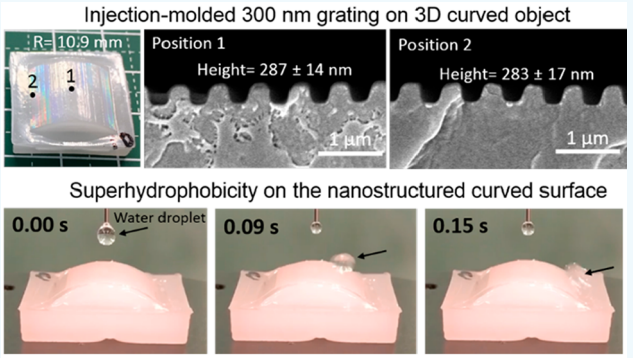

KEYWORDS: *nanoinjection molding, multiscale simulation, superhydrophobic, surface topography, curvature*

1. INTRODUCTION

Controlling surface wetting or nonwetting remains an important material and product design parameter for a wide range of applications. Examples of product performance associated with surface wetting properties are antisweat in devices such as hearing aids and goggles. Generally, wetting properties of polymers are determined by the intrinsic surface chemistry and the surface topography.[1] Surface chemistry determines the intrinsic wettability of the surface while topography acts to enhance or reduce wettability resulting in superhydrophobic,[2] superhydrophobic,[3] or superoleophobic surfaces.[4] The advancement of lithographic techniques has spurred the research and development of interesting topographic designs that span the length scales from micrometer to nanometer, many of which were bioinspired or biomimetic and would have been difficult or not achievable by traditional manufacturing techniques such as molding and surface finishing. A plethora of topographical designs that show enhanced antiwetting surface properties have been reported.[5,6] Even though many real-life applications for antiwetting surfaces extend beyond sheetlike objects, there have been limited reports on the fabrication of antiwetting topographies on geometrically complex, free-form 3-dimensional (3D) objects. Wu et al.[7] reported wettability switching induced by curvature to control water droplet transport. Such control was performed through the curvature adjustment achieved by mechanical pressing onto the flexible microstructured polymer film. Kizilkan et al.[8] reported surface adhesion property change as a function of curvature by bending a microstructured film. Still, the above studies utilized conventional two-dimensional (2D) lithography process to pattern the surface of polymer film and employed continuous application of external stimuli (e.g., mechanical pressing and bending) to maintain a given film distortion/curvature. The main challenge in direct patterning of high-resolution topography onto free-form 3D object lies on one hand the form factor limitation of lithographic techniques

Received: April 3, 2019
Accepted: May 24, 2019
Published: May 24, 2019

DOI: 10.1021/acsapm.9b00312
ACS Appl. Polym. Mater. 2019, 1, 1547−1558

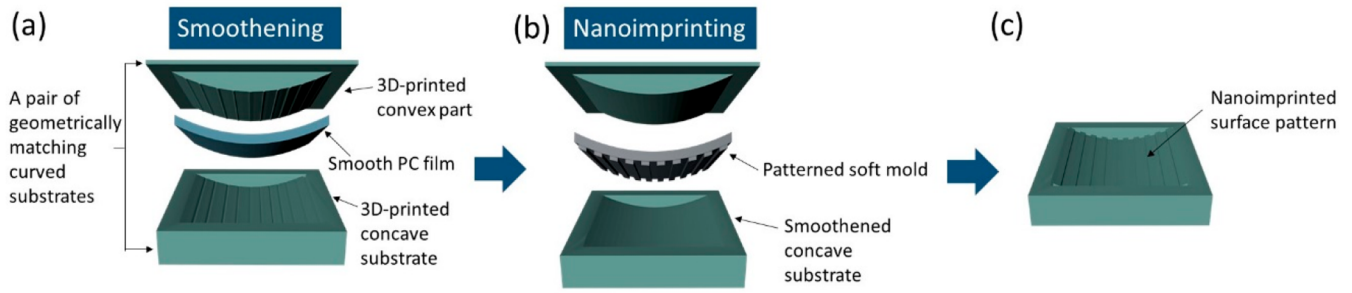

Figure 1. Schematic diagram (not to scale) showing the steps for thermal imprinting on nonplanar polymer substrates. (a) "Blank imprinting" with a nonpatterned polycarbonate film to smoothen the convex and the concave substrates. (b) Thermally imprinting the curved surface with a patterned ETFE. (c) A nanoimprinted curved substrate to be used as the patterned mold insert for injection molding.

and on the other hand the surface resolution limit of traditional object forming techniques.

Among the traditional object forming techniques, injection molding is ubiquitous for manufacturing of free-form 3D products. Today, the resolution of injection molding has been established in the micrometer scale, known as microinjection molding. Microinjection molding produces parts with structural dimensions in micrometers or submicrometers.[9] However, a broader definition of microinjection mold includes molded parts smaller than 1 mm or large molded part consisting of surface feature smaller than 200 μm.[10] Beyond submicrometer resolution, injection molding of compact disc (CD) and digital video disk (DVD) with feature dimensions ranging from 100 to 500 nm has been achieved.[11−13]

Injection molding of thermoplastic polymers with feature spanning millimeter to submicrometer length scale presents new challenges for polymer filling predictions, which are further complicated by nonplanar geometries. A high surface-to-volume ratio in the submicrometer and nanometer features causes high thermal diffusion rate in polymer melt, results in premature solidification of polymer melt, and prevents the complete filling in micro-/nanocavities. Process improvement and optimization via the implementation of *variotherm* mold heating systems,[14−16] heat transfer retardation,[17,18] cavity vacuum pumping systems,[19,20] and antistick coatings[13,21] have been demonstrated to achieve micrometer surface patterns, with a few successes in nanometer surface patterns in a variety of injection-molded polymer sheets. These approaches have been successful in pushing the resolution limit of injection molding primarily through reducing premature solidification, entrapped air, and interfacial effects. Summaries of these approaches can be found in the Supporting Information (Table S1).

Publications on injection molding of superhydrophobic surface topography are mostly limited to flat objects[22−24] and one recent work on hierarchical microstructure on curvature.[25] Nevertheless, there is a dearth of studies about topographic patterning on curved surfaces via injection molding due to the lack of robust and efficient design tools to optimize the process parameters to achieve high-resolution nano-/micropatterns on curved surfaces. Commercial software tools, such as Moldflow and Moldex3D, have been widely used for simulation of polymer flow in injection molding. However, these simulation tools are developed based on macroscopic dimensions.[26] In the research field of nanoimprinting, simulation of high-resolution polymer in asymmetrical cavities has been reported.[27] Nevertheless, the replication mechanisms between injection molding and nanoimprinting are substantially different. In the injection-molding process, molten polymer is injected into the mold and then transitions into rubbery and glassy states upon cooling, whereas in nanoimprinting of thermoplastics a polymer at room temperature is heated to the rubbery state while in contact with a planar mold (typical nanoimprinting temperature is 30−50 deg higher than the glass transition temperature). Furthermore, in the nanoimprinting process, the temperature and pressure uniformity are well-maintained (achieved through special hardware design and software control), while in injection molding, polymer in the cavities experiences a large temperature change, from the considerably high melting temperature to the rubbery and cooling temperature. The effects of large temperature gradient and nonuniform pressure in the injection-molding process can be amplified in multiscale mold cavities. To simulate the injection-molding processes that replicate nano-/microscale patterns on curved surfaces requires a large number of meshes and elements and also multiscale mesh grading to represent the features in both nano-/microscales and macroscales, which makes the simulations of these multiscale injection-molding processes computationally unaffordable. In this work, we report a multiscale modeling approach to simulate the injection-molding processes to achieve submicrometer surface texture on curved polymeric objects. The injection-molded surface topography on macroscopically curved objects was subsequently investigated for surface superhydrophobicity and antiwetting performance.

2. EXPERIMENTAL SECTION

2.1. Fabrication of Nonplanar Mold Inserts with Submicrometer Surface Pattern. A reported hybrid process of 3D printing and nanoimprinting was employed to fabricate polymer-based nonplanar mold inserts with high-resolution surface patterns.[28] The design rationale for mold inserts is described in the Supporting Information. The mold inserts with molding surface upward were printed using a "Digital ABS" mixture of RGD515 and RGD535 photocurable resin (purchased from Stratasys), using a multimaterial PolyJet 3D printer (Stratasys J750). Print lines were along the direction of injection flow path. Curved 3D-printed objects subsequently went through a two-step thermal imprint process (Figure 1). In the first step (i.e., surface smoothening), an optical grade polycarbonate (PC) film (from Innox, Japan) was sandwiched between the geometrically matched concave and convex substrates; a "blank imprinting" was performed at 20 bar and 100 °C for 5 min. All imprinting processes were performed by using a Nanonex NX-2006) (Figure 1a). In the second step (i.e., surface patterning on mold inserts), an ethylene tetrafluoroethylene (ETFE) sheet, Fluon (Asahi Glass Co.), with thickness of 100 ± 10 μm was used as a flexible mold. The ETFE flexible mold was imprinted with patterned Si mold (uniform grating: width = 300 nm, pitch = 600 nm, height = 300 nm)

DOI: 10.1021/acsapm.9b00312
ACS Appl. Polym. Mater. 2019, 1, 1547−1558

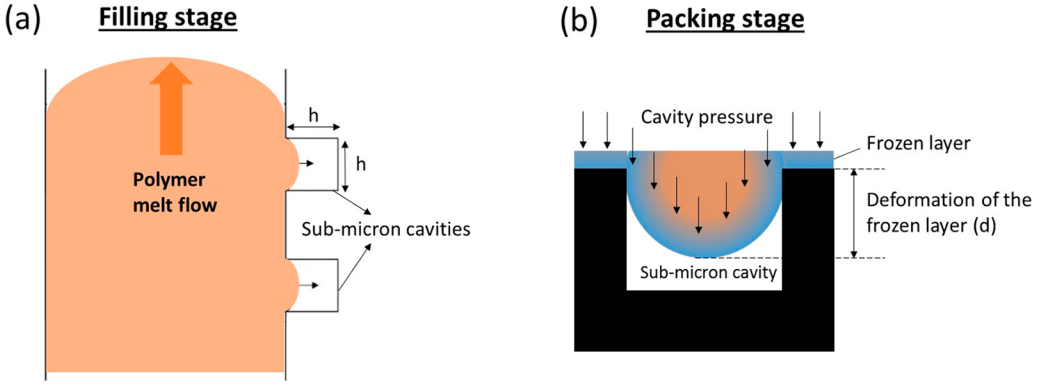

Figure 2. (a) Schematic showing melt flow during filling stage, in which the molten polymer fills the macroscopic cavity while the melt flow stagnates at the entrance of submicrometer cavities. (b) Schematic representation (not to scale) of the filling into submicrometer cavity during packing stage based on a frozen layer deformation model. The blue and orange colors indicate the frozen layer and the melt, respectively.

and served as a soft mold for imprinting on the curved substrates (see Figure 1b). The imprinted curved substrate would be used as the mold insert (Figure 1c) for subsequent injection-molding experiments and will be referred as the imprinted mold insert. The imprinted mold insert was then coated with a layer of Au−Pd (~8 nm) by using a JEOL JFC-1200 coater (plasma current: 30 mA; exposure time: 35 s). Subsequently, an antiadhesion coating, 1*H*,1*H*,2*H*,2*H*-perfluorodecyltrichlorosilane (FDTS), was added using a Nanonex silane coater.

The high-aspect-ratio pillar structure was fabricated by using a commercially available anodized aluminum oxide (AAO, Shangmu Tech.). The AAO template is an 80 μm thick sheet with hexagonally arranged pores 200−300 nm in width, 2 ± 0.5 μm in depth, and 400−450 nm interpore distance. AAO templates were first treated with FDTS at 120 °C for 2 h. The digital ABS was put through an annealing process to strengthen the mold insert and increase its heat deflection temperature (HDT) from 60 to 95 °C. Subsequently, the silanized AAO sheet was mechanically pressed onto the digital ABS curved surface to maintain a given curvature.

2.2. Injection Molding of Curved Objects with Submicrometer Surface Texture. The injection-molding process was performed by using the Babyplast 6/10P microinjection-molding machine, and the material was polypropylene (PP, Cosmoplene AX161). PP was conditioned in an oven at 80 °C for 6 h before injection molding. The patterned mold insert was inserted at the center of the steel mold base, and the photographs of inserts used for the injection molding of grating and pillar structures are shown in Figure S1. Representative images of a nanoimprinted curved mold insert (R = 28.6 mm) in Digital ABS are shown in Figure S2. Injection-molding experiments were conducted at a constant flow rate of 6.157 $cm^3\ s^{-1}$, resulting in a filling time of about 0.4 s and a holding time of 10 s. The formation of knit lines was avoided by setting the melt temperature to 210 °C. The injection pressure was 20 MPa. For each set of parameters, 15 shots were conducted, but only the last three shots were used for subsequent characterization.

2.3. SEM Imaging. A JEOL field emission scanning electron microscope (SEM), JSM 6700F, was used for all SEM imaging characterization. All samples were coated with Au−Pd using the same conditions as described in section 2.1. Pattern geometry measurements were performed using ImageJ software.

2.4. Simulation. A multiscale simulation method was developed to model bulk polymer melt flow and submicrometer scale filling in the injection-molding process. The macroscale flow properties (i.e., time- and location-dependent cavity pressure and polymer surface temperature) for filling and packing (holding) stages were analyzed by using the commercial software Moldflow. In Moldflow, a three-noded triangular element was employed for meshing the parts. Different geometries (flat and curved) used for the simulation are shown in Figure S3a. The macroscale filling was simulated without the submicrometer cavities. The analysis sequence was modeled as fill and pack. Thermoplastics injection-molding solver parameters (dual domain) were used. The material properties of molding polymer (PP) are adopted from the software material library, whereby melt density, solid density, and Poisson's ratio are 0.80 g/cm^3, 1.01 g/cm^3, and 0.392, respectively. The viscosity of PP as a function of shear rate and temperature is shown in Figure S3b. The melt temperature was set as 210 °C. The filling, holding, and cooling time (100 s) for the simulations in Moldflow were set as the same as those in the experiments. The flow was modeled in 3D meshes using Navier−Stokes equations for non-Newtonian viscosity. The viscoelastic effects were considered in the simulation. The density is not constant at high pressure, which can be seen from the volumetric shrinkage change in Figure S3c. The pressure and temperature for a particular node were obtained through simulation as a function of time. The average pressure during the holding stage was calculated by integrating the pressure with time and then dividing it by the time taken for the holding pressure to drop to zero. The corresponding average temperature was also obtained by using the same method. A microscale analytical model was constructed to investigate the filling of submicrometer cavities by the deformation of a frozen zone during the packing stage. The local submicrometer cavity filling behavior was simulated by taking the results of macroscale flow (cavity pressure and surface temperature) obtained from Moldflow as the boundary conditions in the inlet of submicrometer cavity.

2.5. Water Contact Angle and Sliding Angle Measurements. Static water contact angle (CA) measurement was performed by using a Kino SL200 KS goniometer. The static water contact angle was obtained by using 20 μL of deionized water droplet. For measurement on curved patterned surface, a water droplet was deposited at the apex of a curved surface such that the droplet is symmetrically centered. CA values were measured by using the integrated goniometer software. The sliding angle (SA) was measured at the onset of water droplet (20 μL) rolling off when the sample is tilted.

3. RESULTS AND DISCUSSION

3.1. A Modified Model for Multiscale Simulation of Submicrometer Structure Replication. Polymer filling in submicrometer cavities was simulated by obtaining macroscale flow values of cavity pressure and polymer surface temperature from Moldflow for the inlet boundary of the submicrometer cavity. Two assumptions were made: (i) The density and viscosity of the molten polymer were set as constant because changes to bulk density and viscosity are only a concern when the cavity dimension falls below 100 nm.[29,30] (ii) There is minimal spatial variation over the inlet boundary of submicrometer cavities; hence, pressure and temperature were set as constant. Therefore, only temporal variations are considered at the cavity boundary.

DOI: 10.1021/acsapm.9b00312
ACS Appl. Polym. Mater. 2019, 1, 1547−1558

The polymer flow into the multiscale mold cavity is divided into two stages: the filling and packing (holding) stage. In the filling stage, the polymer melt fills the macroscopic cavity where the resistance to the flow front is low (Figure 2a). When polymer melt reaches the submicrometer cavities on the mold, the melt front rapidly cools, and the melt flow almost stagnates at the opening of the submicrometer cavities. Polymer filling into the submicrometer cavities can be described by a known pressure-driven flow (in the Supporting Information), which takes into consideration the capillary pressure of the polymer melt, polymer melt viscosity, and air pressure and predicts that polymer melt can fill only a very short distance (~2 nm) in the submicrometer cavities. Hence, the filling of polymer in the submicrometer cavity occurs mainly during the packing stage (Figure 2b). The packing stage occurs when the molten polymer front reaches the submicrometer cavities, at which point substantial temperature reduction occurs, and the polymer transitions into a rubbery phase; an analytical model was constructed to simulate rubbery deformation of the polymer under the relevant temperature and pressure. The nomenclature of parameters and their values used in the analytical model are listed in Table 1.

We adopted Yoshii's replication model[40] to simulate deformation of a frozen layer as the mechanism of polymer filling in micro- and nanometer cavities. In keeping with the original convention, the packing depth is termed the filling depth, d, and is expressed by a simple beam bending model (Figure 2b) through eq 1:

$$d = \frac{Ph^4}{32EH^3} \tag{1}$$

where P is cavity pressure simulated from Moldflow, h is feature wall thickness, E is Young's modulus of injected polymer, and H is thickness of frozen layer. As the length scale of the mold cavity decreases, entrapped air pressure, rapid solidification at the cavity wall, and surface tension would become more pronounced, reducing the effective pressure at the entrance of micro-/nanocavity. Hence, the filling distance in the submicrometer cavity during the packing stage in eq 1 was modified to include the parameters of capillary pressure and entrapped air pressure:

$$d = \frac{(P - P_{\text{capillary}} - P_{\text{air}})h^4}{32EH^3} \tag{2}$$

where $P_{\text{capillary}}$ is the capillary pressure induced by surface tension and P_{air} is the entrapped air pressure inside of the cavity.[41] $P_{\text{capillary}}$ can be calculated by

$$P_{\text{capillary}} = -\frac{2\gamma \cos \vartheta}{h} \tag{3}$$

where γ is surface tension of polymer melt and ϑ is the dynamic contact angle between polymer melts and the mold. In our work, $P_{\text{capillary}}$ was calculated to be ~0.066 MPa, which is 3 orders of magnitude smaller than cavity pressure (several tens of megapascals). Although the contribution of capillary pressure induced by surface tension is negligible in the dimension of several hundreds of nanometers (200−300 nm in this case), it is expected to be a significant factor when the cavity dimension is smaller than 100 nm.

The entrapped air pressure is determined by an ideal gas volumetric behavior:[42]

Table 1. Parameters Used in the Analytical Model

parameter	description	units	value
	known parameters		
h	feature wall thickness	nm	300 nm for grating; 250 nm for pillars
E	Young's modulus	MPa	105 and 72 MPa at 130 and 150 °C, respectively[31,32]
α_s	thermal diffusivity of solid polymer	$m^2\ s^{-1}$	7.07×10^{-7}[33]
α_l	thermal diffusivity of polymer melt	$m^2\ s^{-1}$	5.53×10^{-7}[34]
C_l	heat capacity of liquid phase	$J\ g^{-1}\ °C^{-1}$	2.15[35]
C_s	heat capacity of solid phase	$J\ g^{-1}\ °C^{-1}$	1.92[35]
H_f	latent heat of fusion	$J\ g^{-1}$	184[36]
T_l	temperature of liquid phase	°C	210
T_m	melting temperature	°C	160
γ	surface tension of polymer melt	$mN\ m^{-1}$	20[37]
ϑ	contact angle between polymer melt and mold wall	deg	120°[38]
P_1	initial air pressure	MPa	0.05 MPa for the grating that is aligned with the flow direction;[39] 0.1 MPa for pillars
y	constant for a diatomic gas		1.4
V_1	initial space	nm^2	90000 nm^2 for grating; 500000 nm^2 for pillars
	parameters determined by Moldflow		
P	pressure at the entrance of micro-/nanocavity	MPa	results are discussed in the main text
T_s	temperature of solid phase	°C	
	parameters determined by the analytical model		
d	filling depth during the packing stage	nm	
H	thickness of frozen layer	nm	
$P_{\text{capillary}}$	capillary pressure	MPa	
P_{air}	entrapped air pressure	MPa	
t	time	s	

$$P_{\text{air}} = P_1\left(\frac{V_1}{V_2}\right)^y \tag{4}$$

where P_1 and V_1 are the initial pressure and volume and V_2 is the current volume. A schematic of the cross-sectional geometry of the filling of 300 nm grating can be found in Figure S4, with further explanation on the calculations of unfilled space (V_2) and polymer filling percentage based on simulated filling depths (d) and the extent of corner filling.

The frozen layer thickness during the molding process was determined via the following equation:

$$H = 2\lambda\sqrt{\alpha_s t} \tag{5}$$

where λ was obtained by solving eqs 6−8, α_s is the thermal diffusivity of the solid, and t is the time. λ in eq 5 is the solution of the equation[43,44]

DOI: 10.1021/acsapm.9b00312
ACS Appl. Polym. Mater. 2019, 1, 1547−1558

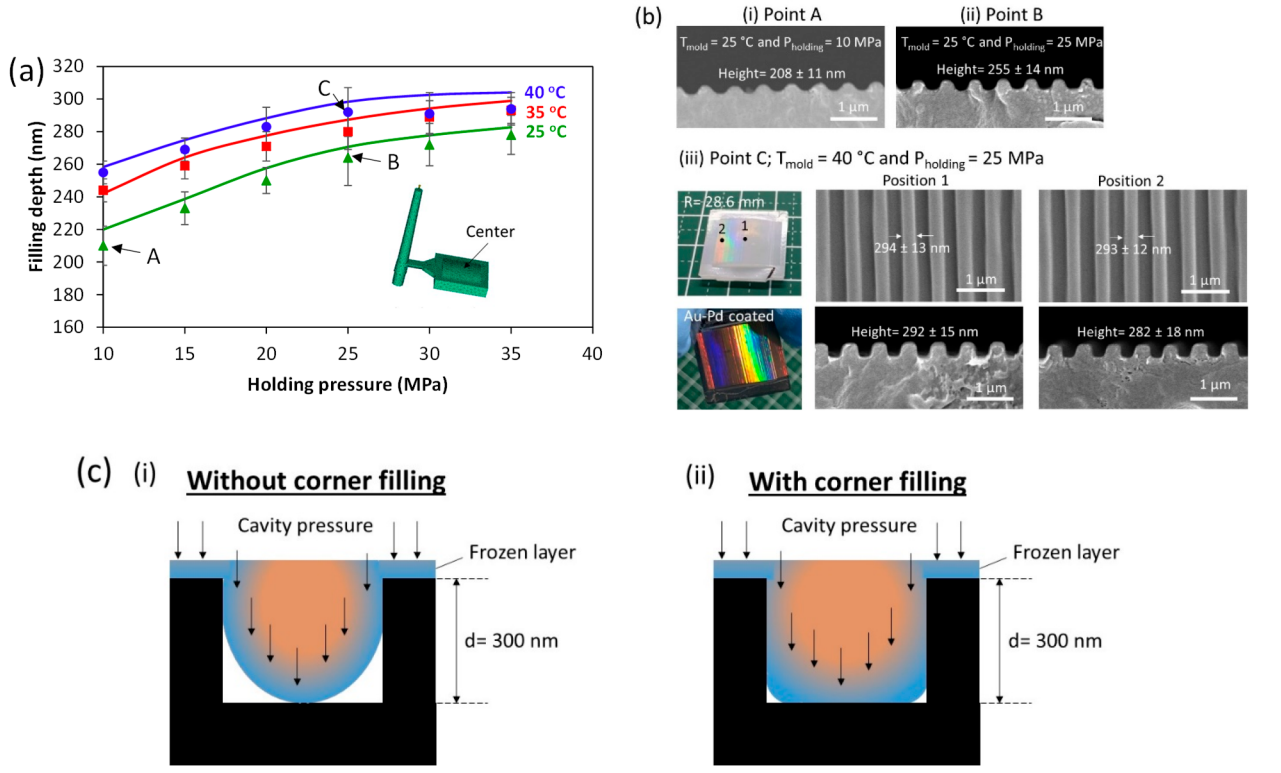

Figure 3. (a) Filling distances of grating structure at the center of the semicylindrical convex surface (R = 28.6 mm) as a function of holding pressure and mold temperatures. The simulation results are expressed in solid curves while the experimental data are shown in symbols. (b) SEM images of top and cross-sectional views of injection-molded grating structure fabricated by different process parameters as indicated in (a) (i.e., points A–C). Photographs of the injection-molded parts (R = 28.6 mm) uncoated and coated with Au–Pd are shown in (iii). (c) Schematic representations (not to scale) of the filling of 300 nm grating (i) without corner filling and (ii) with corner filling during the packing stage based on a frozen layer deformation model. The blue and orange colors indicate the frozen layer and the melt, respectively.

$$\frac{St_l}{\exp(\lambda^2)\,\mathrm{erf}(\lambda)} - \frac{St_s\sqrt{\alpha_s}}{\sqrt{\alpha_l}\,\exp(\alpha_l\lambda^2/\alpha_s)\,\mathrm{erfc}(\lambda\sqrt{\alpha_l/\alpha_s})} = \lambda\sqrt{\pi} \tag{6}$$

where

$$St_l = \frac{C_l(T_l - T_m)}{H_f} \tag{7}$$

$$St_s = \frac{C_s(T_m - T_s)}{H_f} \tag{8}$$

Here, erf and erfc are the error function and complementary error function, respectively, and α_l is the thermal diffusivity of the liquid. C_l and C_s are the heat capacities of the liquid and solid, respectively. H_f is the latent heat of fusion. T_l, T_m, and T_s are the temperatures of liquid phase, melting point, and solid, respectively.

To validate the proposed multiscale modeling approach, two types of surface structures, anisotropic grating and high-aspect-ratio isotropic pillars of submicrometer scale, were investigated for injection molding of PP. The filling depth (or grating height) can be directly measured from the SEM images of cross-sectional view of grating structure, and the experimentally measured filling depths were compared with the simulated filling depths. From Figure 3a, both the simulation and experimental results show the same trend of filling depth for grating at the center of the semicylindrical surface as a function of holding pressure for various mold temperatures. Filling depth of grating at the center of the semicylindrical convex surface (R = 28.6 mm) increases when the mold temperature and holding pressure increase (Figure 3a). The SEM images of the injection-molded grating structure, which were created at various mold temperatures and holding pressures (points A to C in Figure 3a), are shown in Figure 3b. When injection molded at T_{mold} = 25 °C and $P_{holding}$ = 10 MPa, the grating height was measured to be 208 ± 11 nm, lower than then the corresponding grating depth in the mold and the top of the grating was rounded (Figure 3b(i)); these features indicate incomplete filling. Further increase in the holding pressure to 25 MPa improved the filling depth of the grating although the filling depth is still 15% shorter than the mold dimension (Figure 3b(ii)). Maintaining the holding pressure at 25 MPa and now increasing the mold temperature to 40 °C resulted in the highest pattern fidelity (>95% of the mold dimension) as characterized by grating height, width, and shape. As shown in Figure 3b(iii), the squarish shape observed on the tops of the 300 nm grating indicates complete filling with average grating height of 287 nm and width of 294 nm at the center (position 1) and side (position 2). In contrast to nonpatterned surfaces, the entire surface-patterned convex surface presents iridescent color, indicating nearly 100% pattern transfer. It is noteworthy that at a mold temperature of 40 °C the optimal holding pressure was determined to be 25 MPa; further increase in the holding pressure (e.g., 30 and 35 MPa) is not recommended due to an increase molded-in stress caused by overpacking of the rubbery polymer.[45,46]

DOI: 10.1021/acsapm.9b00312
ACS Appl. Polym. Mater. 2019, 1, 1547–1558

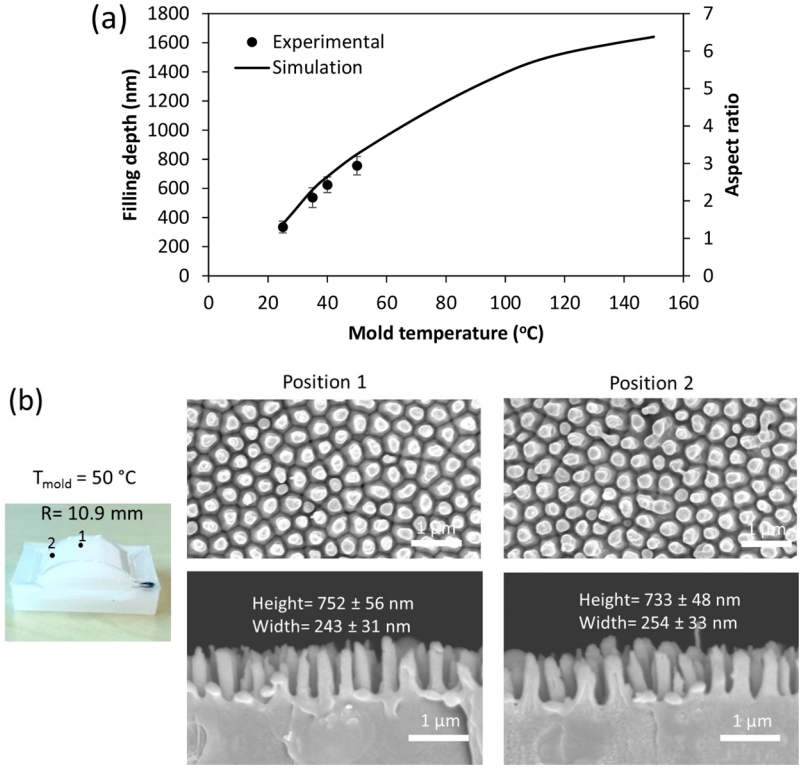

Figure 4. (a) Filling distances of pillar structure at the center of the semicylindrical convex surface (R = 10.9 mm) as a function of mold temperature at a constant holding pressure of 40 MPa. The simulation results are expressed in solid curves while the experimental results are shown in symbols. (b) SEM images of top and cross-sectional views of nanopillar structure on the semicylindrical PP with curvature (R = 10.9 mm).

Unlike the injection molding of micro-/nanostructures using nickel- or silicon-based mold inserts, which were typically conducted at T_{mold} > 100 °C and $P_{holding}$ > 70 MPa,[12,15,20] relatively low range values for T_{mold} (below 50 °C) and $P_{holding}$ (10−40 MPa) were used for injection molding in the current work. Mold inserts made of Digital ABS would undergo deformation when the mold temperature is above its T_g, which is 50 °C. An overly high holding pressure risks physical damage to the mold insert. Similarly, the same process parameters (T_{mold} = 40 °C and $P_{holding}$ = 25 MPa) successfully replicated 300 nm grating on a semicylindrical part with a higher degree of curvature (Figure S5).

Schematic representations of the cross-sectional geometry of the filling of 300 nm grating without and with corner filling are illustrated in Figure 3c. At a filling depth of 300 nm, filling into the submicrometer cavity corners would be impeded (Figure 3c(i)) if the entrapped air pressure is comparable to the cavity local pressure during the packing stage. On the other hand, the submicrometer cavity corners can be filled by the effect of cavity pressure (Figure 3c(ii)) when the local pressure sufficiently counteracts the entrapped air pressure. There have been several studies reporting on the implementation of cavity vacuum pumping systems to improve polymer filling in injection molding of micro- and nanometer patterns.[19,20] In those studies, a continuous vacuum was applied in the mold cavity and the runner to remove gases or trapped air during injection molding. Although no cavity vacuum pumping system was used in the present work, the grating structure on the mold insert was aligned with the flow direction, which allows trapped air to escape with the flow during filling.[15,47] In our study, the grating lines on the mold insert were imprinted perpendicular to the curvature so that polymer melt flow direction is aligned with the grating during injection molding. In this study, the effective cavity pressure of a few tens of MPa is high enough to counteract entrapped air pressure, promoting filling into the submicrometer cavity corners (see Figure S6). Additionally, the thickness of the frozen layer decreased when the mold wall temperature was increased to 40 °C. The thicknesses of the frozen layer were calculated to be 66, 55, and 48 nm for T_{mold} = 25, 35, and 40 °C, respectively. Because the frozen layer thicknesses are much smaller than the grating width (300 nm), it can be deformed to fill into the cavity corners under the packing pressure.

The developed simulation model was extended to model the filling depths inside AAO porous structure (250 nm wide and 2 μm deep) as a function of mold temperature. The simulated filling distance (pillar height) at the center of the semicylindrical convex mold insert (R = 10.9 mm) is shown in Figure 4a (solid curve) as a function of mold temperature and constant holding pressure of 40 MPa. The simulation results fall within the range of experimental filling depths, where the filling depth (pillar height) increases with mold temperature. Figure 4b shows the SEM images of injection-molded pillars (aspect ratio of ∼3) processed at a mold temperature of 50 °C. The molded pillars were not perfectly cylindrical but with conical tips, and the pillar height was 700−800 nm, indicating incomplete pore filling. Based on the simulation results, complete filling (filling depth of 1.5 μm) can be achieved at mold temperature above 100 °C. Because the thermally treated digital ABS can only withstand the mold temperature up to 50 °C, the use of other mold insert material with increased thermomechanical stability will be needed for achieving higher aspect ratio (>3) nanostructures.

DOI: 10.1021/acsapm.9b00312
ACS Appl. Polym. Mater. 2019, 1, 1547−1558

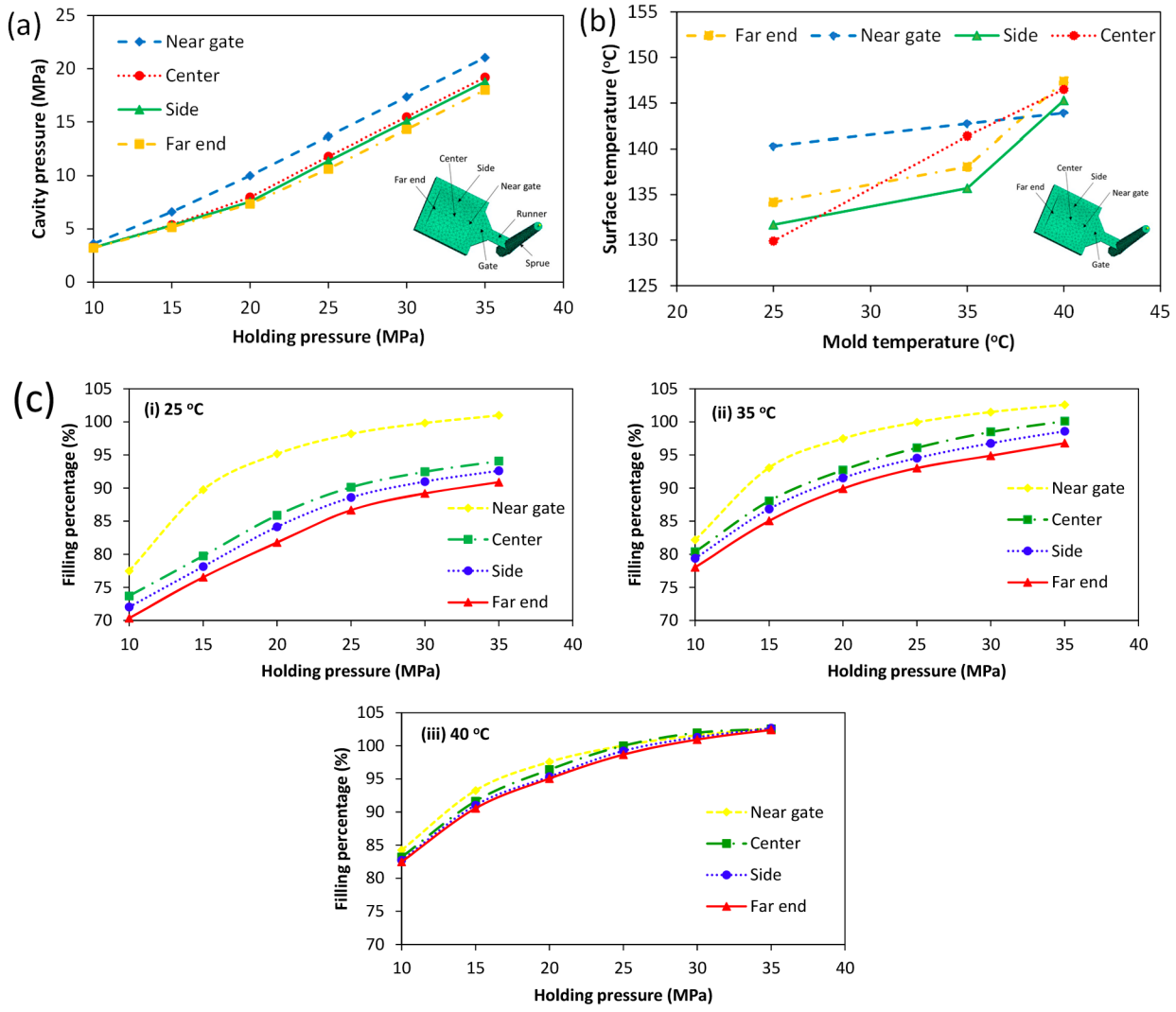

Figure 5. (a) Cavity pressure at various locations on the curved surface (semicylindrical convex, R = 28.6 mm) as a function of holding pressure at a constant mold temperature of 40 °C. (b) Polymer temperatures at various surface locations as a function of mold temperature. (c) Simulated filling percentages of grating structure at various locations on the curved surface (semicylindrical convex, R = 28.6 mm) processed by different mold temperatures and holding pressures. Optimal process parameters (T_{mold} = 40 °C and 25 MPa ≤ $P_{holding}$ ≤ 35 MPa) improve the filling percentage and uniformity over the surface. The lines that connect the data points were added to provide a visual guide.

3.1.1. Replication Uniformity of Submicrometer Texture Over Entire Curved Surface. Polymer melt filling and cooling processes in injection molding are space and time dependent.[48] Melt pressure and temperature variations were not a major concern in most previous studies[12,13,15,47] due to the use of very small mold (<1 cm^2 in patterned area). In this study, the surface patterned mold insert has patterned area = 2.28 cm^2; we further investigated the cavity pressure at various locations on the patterned area. The cavity pressures at various locations on the curved surface (semicylindrical convex, R = 28.6 mm, patterned area = 2.28 cm^2) were simulated as a function of holding pressure at a constant mold temperature of 40 °C (Figure 5a). Cavity pressure is termed the pressure at the entrance of the submicrometer cavity. It is shown that during the packing stage the cavity pressure across the curved surface increases with holding pressure, but at a lower value than the applied holding pressure due to a pressure drop from the sprue. Furthermore, the cavity pressure is higher near the gate but reduces a distance further from the gate. Injected polymer temperatures at various surface locations were also simulated as a function of mold temperature, as shown in Figure 5b. Increasing the mold temperature to 40 °C results in a higher and more uniform temperature over the curved surface with a standard deviation of 1.5 °C. In comparison, a wider polymer temperature distribution with standard deviation of 5 °C was determined for a relatively low mold temperature at 25 °C.

Filling percentages at various locations on the curved surface (semicylindrical convex, R = 28.6 mm) were subsequently simulated to examine the uniformity of the molded grating structure processed at different mold temperatures and holding pressures (Figure 5c). Polymer filling percentage was calculated based on the cross-sectional geometry of 300 nm grating (Figure S4), simulated filling depths (d) and the extent of corner filling. The simulation shows a decrease in filling percentage from the near gate to the far end of the main cavity for all the mold temperatures and holding pressures investigated. Furthermore, it is found that increasing mold temperature to 40 °C and holding pressure to 25−35 MPa can improve the uniformity of filling with a standard deviation of 0.7% (Figure 5c). A sufficiently high cavity pressure (at least 10

DOI: 10.1021/acsapm.9b00312
ACS Appl. Polym. Mater. 2019, 1, 1547−1558

MPa shown in Figure 5a) provided by holding pressures of 25−35 MPa and a narrow temperature distribution for T_{mold} = 40 °C (Figure 5b) are the main factors that contribute to a highly uniform filling.

3.1.2. Effects of Macroscopic Curvature on Replication Fidelity. In addition to the above finding on pressure variation across an array submicrometer mold cavities, pressure variation in injection molding is also affected by the overall geometry in the mold cavity, especially if there is thickness variation in the geometry.[16] To investigate the effect of macroscopic curvature on the pressure variation across mold insert/cavities, all designs investigated have a constant thickness of 4 mm. The simulation results of cavity pressure at the center of the surface during molding of parts with various radii of curvature (semicylindrical and flat) at a mold temperature (40 °C) are shown in Figure 6a as a function of holding pressure. The

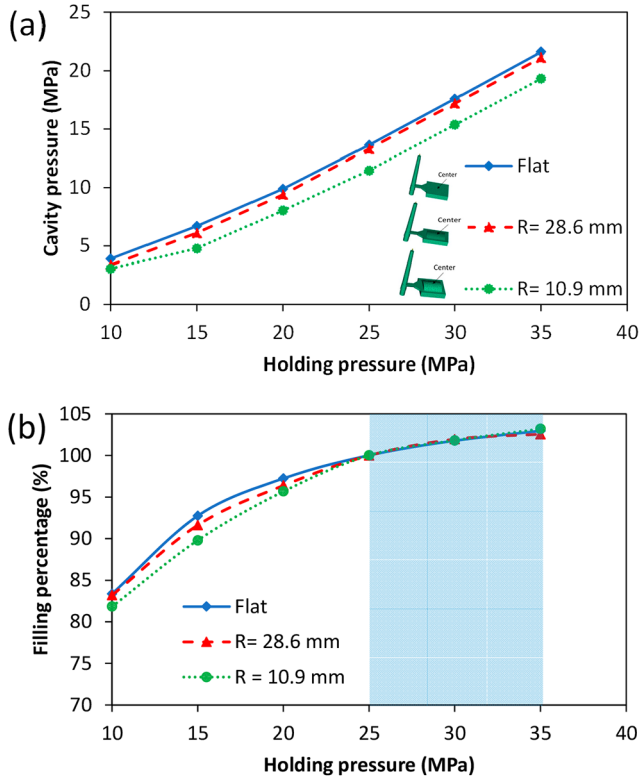

Figure 6. (a) Cavity pressure at the center of the surface with various curvatures (semicylindrical and flat parts) as a function of holding pressure at a constant mold temperature of 40 °C. (b) Simulated filling percentages of grating structure at the center of the surface with various curvatures (semicylindrical and flat parts) as a function of holding pressure at a constant mold temperature of 40 °C. With holding pressures above a critical value of 25 MPa (shaded area), the surface curvatures investigated exhibit a nearly complete filling. The lines that connect the data points were added to provide a visual guide.

cavity pressure was estimated to decrease with increasing degree of curvature. This result could be explained by a more substantial pressure drop with increasing degree of curvature, at which the apex of convex molded part is further away from the gate, leading to a higher resistance to packing flow.

As the injected polymer begins to cool and harden within the mold, not all regions cool at the same rate, especially for parts with changing thickness. In this work, part walls were made uniform in thickness throughout the entire flat and curved surfaces (R = 28.6 mm and 10.9 mm) to minimize uneven cooling of the injected polymer at various locations. Polymer temperatures at the center of the surface were therefore determined to be similar for the flat and various curved geometries.

The simulated filling percentages of grating structure at the center of the surface for various curvatures are shown in Figure 6b. At a mold temperature of 40 °C, the flat surface exhibits higher filling percentage compared to curved samples due to higher cavity pressure. Nevertheless, with holding pressures above a critical value of 25 MPa, the two curved samples investigated (R = 28.6 and 10.9 mm) exhibit nearly complete filling. Although not investigated in this study, cavity pressure is expected to reduce with increasing degree of curvature and higher mold temperature, holding pressure and injection speed may be needed to achieve full pattern replication.

In addition to the extent of filling, demolding is another key factor that governs replication fidelity of the injection-molded parts. FDTS coating on the mold inserts was used to reduce polymer stiction and preserve structure during demolding process. The grating and pillar structures with aspect ratio ranging from 1 to 3 on the convex surfaces (R = 28.6 and 10.9 mm) reported in this work were preserved after demolding. However, at higher aspect ratio and degree of curvature than the ones investigated here, other strategies may be needed such as the introduction of draft angle to the side walls of nanofeatures, use of highly rubbery or elastomeric polymer, and modular mold designed for easy demolding. The simulation model developed here can be extended to investigate other more complicated geometries.

3.2. Characterization of Antiwetting on Curved Surface with Submicrometer Structure. Grating or tilted pillar structures have been effective in introducing anisotropic wetting behavior on planar surfaces.[49,50] The synergy of macroscopic curvature with submicrometer surface structure for wettability tuning is further demonstrated in this work. Wettability of nonpatterned curved surface, as measured by water contact angle, was first investigated as a control study. In Figure 7a, the intrinsic contact angle (CA) on a nonpatterned, flat (degree of curvature, $1/R$ = 0) PP substrate was measured to be 92 ± 1° (mean ± s.d.). On the surface of a semicylindrical object, the curvature is zero along the length of the cylindrical surface. The semicylindrical PP investigated here presents an anisotropic curvature, which results in anisotropic wetting, whereby a substantially different CA is observed at viewing directions orthogonal to each other. In this study, θ_y and θ_x on curved samples are defined as the static CA measured in the direction along the curvature and perpendicular to the curvature, respectively. In the case of semicylindrical convex parts, the higher the degree of curvature, the larger the difference between the two water contact angle, $\Delta\theta = \theta_y - \theta_x$, will be and, hence, the larger the degree of anisotropic wetting.

The 300 nm grating imparts an anisotropic effect to the wetting characteristic with $\Delta\theta$ = 28° for the patterned flat surface, as shown Figure 7b. On curved surfaces, the degree of anisotropic wetting was amplified with introduction of the 300 nm grating structure for a given curvature. For instance, at degree of curvature of 0.09 mm^{-1}, $\Delta\theta$ of the patterned surface was found to be 35°, which is higher than that of nonpatterned surface (21°). The observed increase in apparent CA and a higher degree of anisotropic wetting on the curved surfaces

DOI: 10.1021/acsapm.9b00312
ACS Appl. Polym. Mater. 2019, 1, 1547−1558

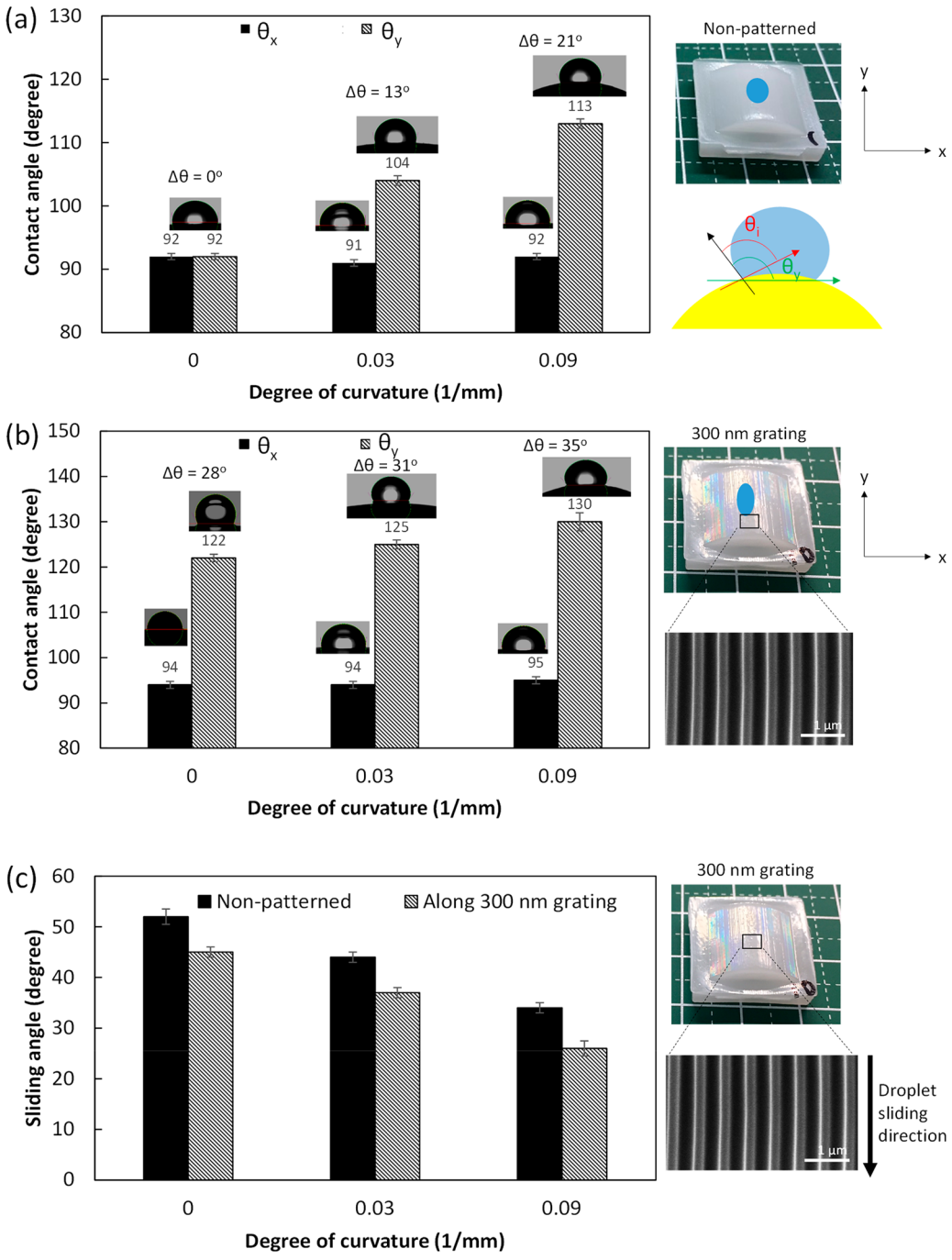

Figure 7. (a) Water contact angles on nonpatterned surfaces with various degree of curvature. Schematic depiction of the intrinsic CA (θ_i) and apparent CA (θ_y) for a liquid drop resting on top of a solid curved surface is shown in the inset on bottom right. (b) Water contact angles on 300 nm grating patterned surfaces with various degree of curvature. (c) Sliding angles on nonpatterned surfaces and 300 nm grating patterned surfaces with various degree of curvature.

with 300 nm grating structure mean that resistance to water flow resistance is reduced. Resistance to flow can be characterized by the sliding angle (SA) which is defined as the tilt angle when the water droplet starts to roll off a surface. Figure 7c shows the SAs of the surface as a function of surface texture and curvature. The volume of water droplet was 20 μL for all experiments. For the nonpatterned, flat PP sample, the SA was the highest, 52 ± 3°, among all samples tested. When increasing the degree of curvature of a nonpatterned surface, the droplet began to roll off at lower SAs of 44 ± 2° and 34 ± 2° on the surfaces with degree of curvature 0.03 and 0.09 mm^{-1}, respectively. For a given surface curvature, 300 nm grating surface shows a lower SA compared to nonpatterned curved surface. For example, at a degree of curvature of 0.09 mm^{-1}, the combination of anisotropic grating and curvature further reduced the SA to 26 ± 3° compared to SA= 34 ± 2° on nonpatterned surface. Water droplet on a curved surface with highly anisotropic solid−liquid contact reduces the energy barrier to roll off along the grating direction, leading to a lower SA. Orthogonal to the grating direction, the droplet was

DOI: 10.1021/acsapm.9b00312
ACS Appl. Polym. Mater. 2019, 1, 1547−1558

pinned to the surface and started to slide off only at ~80° and when the droplet volume was doubled to 40 μL. The 300 nm grating structure on a curved surface was thus demonstrated to allow for anisotropic flow compared to nonpatterned surface.

The isotropic high-aspect-ratio pillar structure (~250 nm wide, aspect ratio ~3) on a curved object (R = 10.9 mm) was used to demonstrate antiwetting performance. The large water wetting contrast between the nonpatterned and high-aspect-ratio pillar-structured surfaces (R = 10.9 mm) is demonstrated in Figure 8a,b. On a nonpatterned surface, a water droplet of

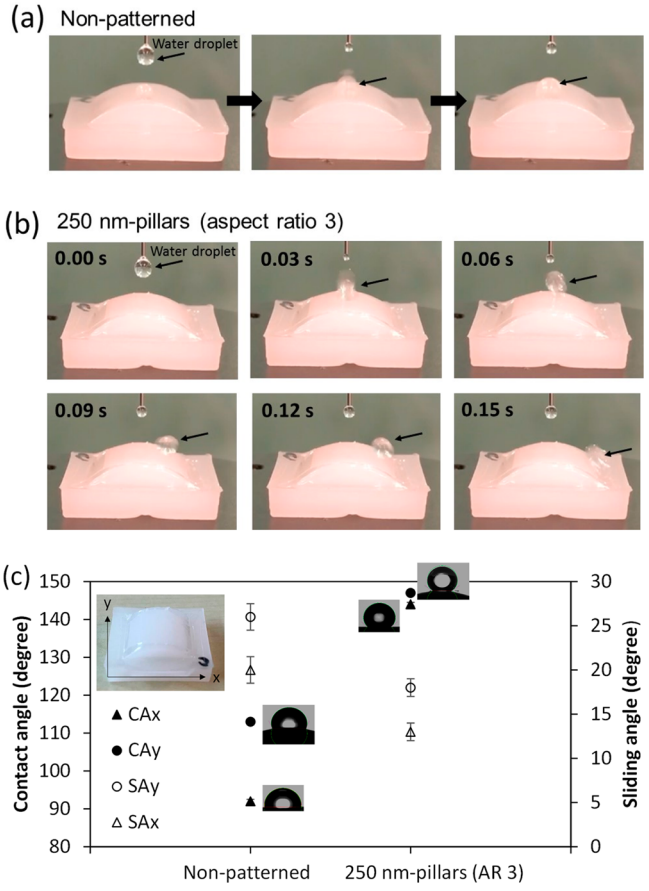

Figure 8. (a) Water droplet pins on the apex of the nonpatterned curved surface (R = 10.9 mm), where the droplet is dropped on. (b) Water droplet rolls off quickly the nanostructured (250 nm pillars with aspect ratio 3) curved surface (R = 10.9 mm). The time sequence is shown in the top left corners of the images. (c) Static contact angles and sliding angles on nonpatterned and nanostructured (250 nm pillars with aspect ratio 3) surfaces (R = 10.9 mm). The contact angles were measured in the direction along the curvature (CA_y) and without curvature (CA_x).

20 μL pinned on the apex of the surface (Figure 8a); conversely, a water droplet rolled off the curved PP whose surface is covered with an array of the 250 nm pillar (Figure 8b). Incorporating the high-aspect-ratio pillar structure formed composite surface between the water droplet and nanostructure, increasing the apparent CA, θ_y, to 147 ± 1.5° and reducing the SA to 13 ± 2° (Figure 8c).

Although not investigated in this study, the robustness of the wetting effect is to a great extent dependent on the mechanical stability of the surface pattern. Generally, high-aspect-ratio micro- and nanoscale pattern such as high-aspect-ratio pillars are more susceptible to damage compared to a low high-aspect-ratio pattern like the grating structure reported in this work. The robustness of the micro- and nanoscale surface pattern can also be enhanced through the use of a polymer with a higher surface hardness and/or by incorporating a protective pattern.[23]

4. CONCLUSIONS

The injection-molding process simulation for multiscale cavities filling was established by the combined Moldflow and pressure-driven deformation modeling. The results showed that the pressure changes during polymer melt filling and the frozen layer deformation during packing greatly influence the degree of filling and the uniformity of submicrometer surface pattern over the macroscopic curvature. For the production of nonplanar PP with 300 nm grating texture, the optimum holding pressure and mold temperature were verified by the experimental results. Nearly 100% yield and pattern fidelity >95% have been achieved over a 2.5 cm^2 semicylindrical PP with surface curvature ranges from 10.9 to 28.6 mm. Furthermore, high-aspect-ratio 250 nm pillars (aspect ratio ~3) on a curved PP were replicated by an AAO mold insert. Simulation also showed that an increase of mold temperature up to 150 °C is necessary for achieving aspect ratio of ~7 for 250 nm pillars. We further reported the combinatorial effects of surface texture and curvature to achieve anisotropic flow and antiwetting effects. Spontaneous dewetting on injection-molded PP has been demonstrated through the synergy of macroscopic curvature and submicrometer surface texture; surface wetting properties can be tuned by simultaneous optimization of macroscopic curvature and high-resolution surface patterns. Because injection molding is a ubiquitous mass production process, achieving the above in injection-molded polymers means that many future products with the desired surface wetting properties can be obtained through geometries and surface texture design optimizations.

■ ASSOCIATED CONTENT

Supporting Information

The Supporting Information is available free of charge on the ACS Publications website at DOI: 10.1021/acsapm.9b00312.

Injection-molding approaches to achieve micro- and nanostructures on flat objects, design consideration of the mold insert, simulation of the filling depth of submicrometer feature during filling stage, photographs of mold inserts for grating and high-aspect-ratio-pillar replication, photograph of a nanoimprinted mold insert with semicylindrical concave surface and corresponding SEM images of top and cross-sectional views of imprinted 300 nm grating, meshed models for macroscale simulation and the dependence of the viscosity of Cosmoplene AX161 on shear rate at different temperatures, volumetric shrinkage of the mold at different times, schematic depiction of the cross-sectional geometric dimensions of the filling of 300 nm grating structure, photographs of injection-molded parts (uncoated and coated with Au−Pd) with semicylindrical convex surface (R = 10.9 mm) and their respective SEM images of top and cross-sectional views of molded 300 nm grating, plot of estimated pressure due to the trapped air vs filling percentage for 300 nm grating (PDF)

DOI: 10.1021/acsapm.9b00312
ACS Appl. Polym. Mater. 2019, 1, 1547−1558

AUTHOR INFORMATION

Corresponding Author

*(H.Y.L.) E-mail hongyee_low@sutd.edu.sg; Ph +65 6499 4612.

ORCID

Wei Li Lee: 0000-0002-9720-3407

Hong Yee Low: 0000-0003-2949-0763

Author Contributions

H.Y.L originated the research direction. W.L.L. designed and performed injection molding experiments and characterization. J.W. contributed to the fabrication of the mold insert recipe. D.W. and Q.G. conducted the simulations. The manuscript was written through contributions of all authors. All authors have given approval to the final version of the manuscript. All authors contributed to the manuscript drafting.

Notes

The authors declare no competing financial interest.

ACKNOWLEDGMENTS

The authors acknowledge the financial support from the Center for Digital Manufacturing and Design (DManD), grant RGDM1630402. The authors also thank Mr. Gan Wee Tze (DManD, SUTD) for his technical assistance in the design of injection mold MUD base.

REFERENCES

(1) De Gennes, P.-G.; Brochard-Wyart, F.; Quéré, D. *Capillarity and Wetting Phenomena: Drops, Bubbles, Pearls, Waves*; Springer Science & Business Media: 2013.

(2) Tian, Y.; Su, B.; Jiang, L. Interfacial Material System Exhibiting Superwettability. *Adv. Mater.* **2014**, *26*, 6872−6897.

(3) Lafuma, A.; Quéré, D. Superhydrophobic States. *Nat. Mater.* **2003**, *2*, 457.

(4) Tuteja, A.; Choi, W.; Mabry, J. M.; McKinley, G. H.; Cohen, R. E. Robust Omniphobic Surfaces. *Proc. Natl. Acad. Sci. U. S. A.* **2008**, *105*, 18200−18205.

(5) Feng, X.; Jiang, L. Design and Creation of Superwetting/Antiwetting Surfaces. *Adv. Mater.* **2006**, *18*, 3063−3078.

(6) Liu, K.; Jiang, L. Bio-Inspired Self-Cleaning Surfaces. *Annu. Rev. Mater. Res.* **2012**, *42*, 231−263.

(7) Wu, D.; Wu, S. Z.; Chen, Q. D.; Zhang, Y. L.; Yao, J.; Yao, X.; Niu, L. G.; Wang, J. N.; Jiang, L.; Sun, H. B. Curvature-Driven Reversible in Situ Switching between Pinned and Roll-Down Superhydrophobic States for Water Droplet Transportation. *Adv. Mater.* **2011**, *23*, 545−549.

(8) Kizilkan, E.; Gorb, S. N. Combined Effect of the Microstructure and Underlying Surface Curvature on the Performance of Biomimetic Adhesives. *Adv. Mater.* **2018**, *30*, 1704696.

(9) Piotter, V.; Mueller, K.; Plewa, K.; Ruprecht, R.; Hausselt, J. Performance and Simulation of Thermoplastic Micro Injection Molding. *Microsyst. Technol.* **2002**, *8*, 387−390.

(10) Yao, D.; Kim, B. Scaling Issues in Miniaturization of Injection Molded Parts. *J. Manuf. Sci. Eng.* **2004**, *126*, 733−739.

(11) Zhang, N.; Byrne, C. J.; Browne, D. J.; Gilchrist, M. D. Towards Nano-Injection Molding. *Mater. Today* **2012**, *15*, 216−221.

(12) Huang, C. Polymeric Nanofeatures of 100 Nm Using Injection Moulding for Replication. *J. Micromech. Microeng.* **2007**, *17*, 1518.

(13) Matschuk, M.; Larsen, N. B. Injection Molding of High Aspect Ratio Sub-100 Nm Nanostructures. *J. Micromech. Microeng.* **2013**, *23*, 025003.

(14) Oh, H. J.; Song, Y. S. Precise Nanoinjection Molding through Local Film Heating System. *RSC Adv.* **2015**, *5*, 99797−99805.

(15) Speranza, V.; Liparoti, S.; Calaon, M.; Tosello, G.; Pantani, R.; Titomanlio, G. Replication of Micro and Nano-Features on Ipp by Injection Molding with Fast Cavity Surface Temperature Evolution. *Mater. Des.* **2017**, *133*, 559−569.

(16) Masato, D.; Sorgato, M.; Lucchetta, G. Analysis of the Influence of Part Thickness on the Replication of Micro-Structured Surfaces by Injection Molding. *Mater. Des.* **2016**, *95*, 219−224.

(17) Park, S.; Lee, W.; Moon, S.; Yoo, Y.; Cho, Y. Injection Molding Micro Patterns with High Aspect Ratio Using a Polymeric Flexible Stamper. *eXPRESS Polym. Lett.* **2011**, *5*, 950−958.

(18) Kim, S.; Jeong, J.; Youn, J. Nanopattern Insert Molding. *Nanotechnology* **2010**, *21*, 205302.

(19) Yokoi, H.; Han, X.; Takahashi, T.; Kim, W. Effects of Molding Conditions on Transcription Molding of Microscale Prism Patterns Using Ultra-High-Speed Injection Molding. *Polym. Eng. Sci.* **2006**, *46*, 1140−1146.

(20) Liou, A.-C.; Chen, R.-H. Injection Molding of Polymer Micro- and Sub-Micron Structures with High-Aspect Ratios. *Int. J. Adv. Manuf. Technol.* **2006**, *28*, 1097−1103.

(21) Stormonth-Darling, J. M.; Pedersen, R. H.; How, C.; Gadegaard, N. Injection Moulding of Ultra High Aspect Ratio Nanostructures Using Coated Polymer Tooling. *J. Micromech. Microeng.* **2014**, *24*, 075019.

(22) Michaeli, W.; Schongart, M.; Klaiber, F.; Beckemper, S. Production of Superhydrophobic Surfaces Using a One-Step Variothermal Injection Moulding Process. *Micro Nanosyst.* **2011**, *3*, 222−225.

(23) Huovinen, E.; Takkunen, L.; Korpela, T.; Suvanto, M.; Pakkanen, T. T.; Pakkanen, T. A. Mechanically Robust Superhydrophobic Polymer Surfaces Based on Protective Micropillars. *Langmuir* **2014**, *30*, 1435−1443.

(24) Yamaguchi, M.; Sasaki, S.; Suzuki, S.; Nakayama, Y. Injection-Molded Plastic Plate with Hydrophobic Surface by Nanoperiodic Structure Applied in Uniaxial Direction. *J. Adhes. Sci. Technol.* **2015**, *29*, 24−35.

(25) Mielonen, K.; Suvanto, M.; Pakkanen, T. Curved Hierarchically Micro-Micro Structured Polypropylene Surfaces by Injection Molding. *J. Micromech. Microeng.* **2017**, *27*, 015025.

(26) Yao, D.; Kim, B. Simulation of the Filling Process in Micro Channels for Polymeric Materials. *J. Micromech. Microeng.* **2002**, *12*, 604.

(27) Rowland, H. D.; King, W. P.; Sun, A. C.; Schunk, P. R. Simulations of Nonuniform Embossing: The Effect of Asymmetric Neighbor Cavities on Polymer Flow During Nanoimprint Lithography. *J. Vac. Sci. Technol., B: Microelectron. Process. Phenom.* **2005**, *23*, 2958−2962.

(28) Wu, J.; Lee, W. L.; Low, H. Y. Nanostructured Free-Form Objects Via a Synergy of 3d Printing and Thermal Nanoimprinting. *Global Challenges* **2019**, *3*, 1800083.

(29) Xu, B.; Ooi, K.; Wong, T.; Liu, C. Study on the Viscosity of the Liquid Flowing in Microgeometry. *J. Micromech. Microeng.* **1999**, *9*, 377.

(30) Eringen, A. C.; Okada, K. A Lubrication Theory for Fluids with Microstructure. *Int. J. Eng. Sci.* **1995**, *33*, 2297−2308.

(31) Zhou, Y.; Mallick, P. Effects of Temperature and Strain Rate on the Tensile Behavior of Unfilled and Talc-Filled Polypropylene. Part I: Experiments. *Polym. Eng. Sci.* **2002**, *42*, 2449−2460.

(32) Zhou, Y.; Mallick, P. Effects of Temperature and Strain Rate on the Tensile Behavior of Unfilled and Talc-Filled Polypropylene. Part Ii: Constitutive Equation. *Polym. Eng. Sci.* **2002**, *42*, 2461−2470.

(33) Weidenfeller, B.; Höfer, M.; Schilling, F. R. Thermal Conductivity, Thermal Diffusivity, and Specific Heat Capacity of Particle Filled Polypropylene. *Composites, Part A* **2004**, *35*, 423−429.

(34) Yánez, G.; Rodríguez-Pérez, M.; Almanza, O. Ldpe and Pp Thermal Diffusivity in Molten State. *Ingeniería e Investigación* **2013**, *33*, 5−8.

(35) Gaur, U.; Wunderlich, B. Heat Capacity and Other Thermodynamic Properties of Linear Macromolecules. Iv. Polypropylene. *J. Phys. Chem. Ref. Data* **1981**, *10*, 1051−1064.

(36) Currie, J. A.; Petruska, E.; Tung, R. In *Analytical Calorimetry*; Springer: 1974; pp 569−577.

DOI: 10.1021/acsapm.9b00312
ACS Appl. Polym. Mater. 2019, 1, 1547−1558

(37) Kwok, D.; Cheung, L.; Park, C.; Neumann, A. Study on the Surface Tensions of Polymer Melts Using Axisymmetric Drop Shape Analysis. *Polym. Eng. Sci.* **1998**, *38*, 757−764.
(38) Grundke, K.; Uhlmann, P.; Gietzelt, T.; Redlich, B.; Jacobasch, H.-J. Studies on the Wetting Behaviour of Polymer Melts on Solid Surfaces Using the Wilhelmy Balance Method. *Colloids Surf., A* **1996**, *116*, 93−104.
(39) Tada, K.; Fukuzawa, D.; Watanabe, A.; Ito, H. Numerical Simulation for Flow Behaviour on Micro-and Nanomoulding. *Plast., Rubber Compos.* **2010**, *39*, 321−326.
(40) Yoshii, M.; Kuramoto, H.; Ochiai, Y. Experimental Study of the Transcription of Minute Width Grooves by Injection Molding (Ii). *Polym. Eng. Sci.* **1998**, *38*, 1587−1593.
(41) Kim, D. S.; Lee, K.-C.; Kwon, T. H.; Lee, S. S. Micro-Channel Filling Flow Considering Surface Tension Effect. *J. Micromech. Microeng.* **2002**, *12*, 236.
(42) Griffiths, C.; Dimov, S. S.; Scholz, S.; Tosello, G. Cavity Air Flow Behavior During Filling in Microinjection Molding. *J. Manuf. Sci. Eng.* **2011**, *133*, 011006.
(43) Hu, H.; Argyropoulos, S. A. Mathematical Modelling of Solidification and Melting: A Review. *Modell. Simul. Mater. Sci. Eng.* **1996**, *4*, 371.
(44) Azaïez, M.; Jelassi, F.; Mint Brahim, M.; Shen, J. Two-Phase Stefan Problem with Smoothed Enthalpy. *Commun. Math. Sci.* **2016**, *14*, 1625−1641.
(45) Guevara-Morales, A.; Figueroa-López, U. Residual Stresses in Injection Molded Products. *J. Mater. Sci.* **2014**, *49*, 4399−4415.
(46) Azaman, M.; Sapuan, S.; Sulaiman, S.; Zainudin, E.; Khalina, A. Optimization and Numerical Simulation Analysis for Molded Thin-Walled Parts Fabricated Using Wood-Filled Polypropylene Composites Via Plastic Injection Molding. *Polym. Eng. Sci.* **2015**, *55*, 1082−1095.
(47) Zhang, N.; Chu, J.; Byrne, C. J.; Browne, D.; Gilchrist, M. Replication of Micro/Nano-Scale Features by Micro Injection Molding with a Bulk Metallic Glass Mold Insert. *J. Micromech. Microeng.* **2012**, *22*, 065019.
(48) Park, K.; Lee, S.-I. Localized Mold Heating with the Aid of Selective Induction for Injection Molding of High Aspect Ratio Micro-Features. *J. Micromech. Microeng.* **2010**, *20*, 035002.
(49) Zhang, F.; Low, H. Y. Anisotropic Wettability on Imprinted Hierarchical Structures. *Langmuir* **2007**, *23*, 7793−7798.
(50) Chen, C. M.; Yang, S. Directed Water Shedding on High-Aspect-Ratio Shape Memory Polymer Micropillar Arrays. *Adv. Mater.* **2014**, *26*, 1283−1288.

DOI: 10.1021/acsapm.9b00312
ACS Appl. Polym. Mater. 2019, 1, 1547−1558